PERGAMON

International Journal of Heat and Mass Transfer 45 (2002) 4793–4808

International Journal of HEAT and MASS TRANSFER

www.elsevier.com/locate/ijhmt

Sharp-interface simulation of dendritic solidification of solutions

H.S. Udaykumar *, L. Mao

Department of Mechanical Engineering, University of Iowa, Iowa City, IA 52242, USA

Received 11 March 2002; received in revised form 7 May 2002

Abstract

A numerical method is developed for the simulation of solidification of solutions/alloys. The heat and species transport equations are solved with appropriate interface conditions. The interface shape and thermal and solutal fields are calculated in a fully coupled manner. The effects of capillarity are included in the interfacial dynamics. The present mixed Eulerian–Lagrangian framework treats the immersed phase boundary as a *sharp* solid–fluid interface and a conservative finite-volume formulation allows boundary conditions at the moving surface to be exactly applied. We first compare the planar growth results with published one-dimensional numerical results. We then show that the method can compute the breakdown of the solid–liquid interface due to the Mullins–Sekerka instability. The dendritic growth of the crystals under various growth parameters is computed.

1. Introduction

There is continuing interest in the development of techniques for simulation of flow and heat transfer around immersed solid boundaries on fixed Cartesian grids. Such methods avoid problems associated with grid generation to conform to the shapes of the evolving solid–liquid boundaries. This is advantageous in computing flows in the presence of embedded solid boundaries which may be complex in shape, arranged in such a way that the flow domain is highly convoluted, or execute motions that deform the flow domain to a very large extent. Such fixed-grid Eulerian methods, classified as immersed boundary [1] or immersed interface [2] methods, may treat the embedded solid boundaries and their interactions with the flowfield in many different ways. A subclass of such methods, which treat the solid–liquid boundary as sharp entities, while still employing a Cartesian grid, has been developed in recent years by several researchers [3–5]. This "sharp-interface" method has been applied to compute the diffusion-controlled growth of unstable phase boundaries [4–6] and fluid flow around fixed [7] and moving [6,8] immersed solid boundaries. This method was also shown to compute the dendritic growth of pure materials in agreement with morphological stability theory [6]. In each case, the method was shown to compute the field equations to second-order accuracy, allowing capture of unsteady and viscous effects.

In this paper, a mixed Eulerian–Lagrangian methodology is extended to include heat and species transport and to track the evolution of freeze fronts in aqueous solutions, alloys and other impure materials where the solidification occurs from the liquid phase. The particular application targeted by this paper is the freezing of solutions used in the cryopreservation of cells and tissue [9], where long-term storage of biological material is sought by freezing at low temperatures. At such low temperatures, physiological processes are slowed or suspended, and thus the phenomena of importance are reduced to physical transport of heat, water and solute. The primary factors controlling cell response to freezing are the cooling rate and temperatures imposed on the cell. Thermodynamics of aqueous solutions dictates that when a solution is cooled ice will precipitate out leaving the remaining solution more concentrated in solute (salts such as NaCl in the human cell and

* Corresponding author. Tel.: +1-319-384-0832; fax: +1-319-335-5669.

E-mail address: ush@icaen.uiowa.edu (H.S. Udaykumar).

0017-9310/02/$ - see front matter
PII: S0017-9310(02)00194-1

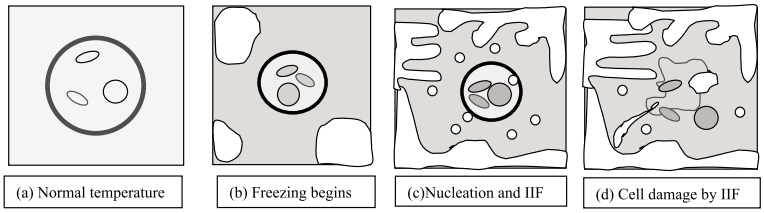

Fig. 1. Illustration of cell death due to IIF. (a) Cell immersed in an isotonic medium. (b) Formation of extracellular ice during cooling. (c) Ice begins to engulf the cell. Water leaves the cell causing shrinkage of cell. Nuclei form in and out of cell. (d) IIF results in cell death.

surrounding tissue [10,11], as given by the phase diagram of the mixture. Therefore, as illustrated in Fig. 1(a), suppose that the cell is initially suspended in an isotonic solution (i.e. the salt concentration in the cell and the surrounding medium are equal). When the mixture is cooled, due to thermodynamic effects [12], ice will first form in the *extracellular* solution (Fig. 1(b)). As the extracellular ice crystals grow, the cell finds itself in surroundings with increasing solute concentration (i.e. in a hypertonic medium). This non-equilibrium situation propels water molecules out of the cell (exosmosis) through the semi-permeable cell membrane [13], thus shrinking (dehydrating) the cell. The key to cell survival is the rate at which cooling is done. If cooling is too rapid, water molecules cannot leave the cell at a rapid enough rate; as the temperature drops ice begins to form inside the cell (Fig. 1(d)). Thus, the intracellular ice formation (IIF) mechanism [14–16] of cell death is imminent. Intracellular ice crystals damage the cell and it will not survive the freeze-thaw process. If the cooling is too slow, then water will leave the cell too slowly, so that the cell will find itself in an increasingly hypertonic environment for longer durations, which again imperils the cell. This is death due to "solution effects" [11]. Cell death can be delayed/prevented by controlling the two effects, i.e. rate of water loss from the cell and increase in the concentration of solute (tonicity) of the surrounding medium.

It is clear that better control of cryopreservation processes calls for ability to quantify the freezing response of the cell. Previous work in analysis of response of the cell to freezing has not accounted in sufficient detail for the extracellular solidification processes. Typically, planar ice fronts succumb to the Mullins–Sekerka instability [17] and assume the form of deep cells or highly branched dendrites. Most analyses to date [10,12,16,18] have assumed that the cell is immersed in an extracellular solution of uniform composition, as dictated by the (spatially uniform) temperature field via a phase diagram. This does not represent the actual condition experienced by a cell that is progressively engulfed by a non-planar ice front, because the advancing ice front carries ahead of it a solute boundary layer whose extent depends on the front velocity. Therefore, while transport of latent heat release during ice formation can be justifiably assumed to occur rapidly, the same does not apply for solute transport.

Several experimental efforts have revealed that the morphology of the ice that attacks the cell can assume cellular or dendritic forms [19]. The cell survivability is also influenced by the morphological features [20]. Kourosh et al. [21] and Koerber and coworkers [22,23] have quantified the temperature and solutal fields that arise when the freezing front assumes cellular morphology under conditions that apply during cryotreatment of cells. Such data are critical to quantify and predict the actual conditions experienced by a cell that is progressively engulfed by a non-planar ice front. The advancing ice front carries ahead of it a solute boundary layer whose extent depends on the front velocity. The egress of water is controlled by the differences in the solutal concentration across the cell membrane. Takamatsu and Rubinsky [20] have convincingly demonstrated the effects of such solute microsegregation in the unfrozen solution. They showed that cells trapped in the solute-rich interdendritic grooves in the mushy (solid–liquid two phase) zone suffer solution effects injury. There has been some previous work on calculating the extent of the solute boundary layer and instability phenomena in the context of freezing of solutions relevant to cryobiology. However, these have been restricted to one-dimensional (1-D) analyses [23–26]. Stability analysis and analytical prediction of non-planar interface morphologies in aqueous systems has also been performed [21,27]. In particular, Kourosh et al. [21] have considered the growth of dendrites in salt solutions by obtaining solutions of crystals in the basal and tip regions and matching these solutions to obtaining a composite representation of the growing crystal. In the thesis by Studholme [28], propagation of a 1-D freezing front was computed by including the instability mechanism due to constitutional supercooling. However, in order to truly understand the interaction of extracellular ice with biological materials, particularly cells, and to quantify the thermo-solutal environment around the cell during freezing, direct numerical simulation of microscale solidification phenomena will be of immense value. A first step in this direction is to develop a capability to

simulate the advance of the solidification front in a freezing aqueous solution in which the cell is suspended. This paper describes such an effort.

The methodology described in this paper is generally applicable to the study of solidification of impure materials, including alloys and solutions. The key feature of the method is the sharp-interface treatment. While there has been a great deal of progress in numerical simulation of cellular and dendritic crystal growth in pure and impure materials, particularly using the phase-field method [29–32], the method presented here affords several distinct advantages. These arise due to the fact that the interface is treated as a sharp entity, so that:

1. The material property jumps at the interface, such as the large jump in the solute diffusivity in passing from the solid to the liquid are treated as discontinuous.
2. The solute partition coefficient determines the concentration gap at the solid–liquid interface and this is explicitly supplied via the boundary conditions at the front in calculating the solute concentration in the two phases. Therefore no smearing of the solute field at the interface results.
3. The capillarity term is included in coupling the interface temperature *and* species at the exact front location (see Eq. (5) below). The coupling is effected in such a manner that a stable implicit time-stepping scheme is developed.
4. A conservative finite-volume formulation can be arrived at, without mixing the phases in each control volume, i.e. the solid and liquid regions are treated as separate domains.
5. Although the current algorithm has been implemented with an interface tracking procedures using curves and markers, it is possible to implement the same with any interface capturing method that allows sharp-interface shape calculations, such as the level-set method [3,33,34]. Such hybrid methods have been employed for dendritic solidification in pure materials but have not yet been employed for impure materials as in the present paper.

Computations of dendritic growth are fairly routine nowadays and there are several approaches for obtaining such solutions. The most widely used method is the phase-field approach [30,32,35] and 3-D computations [29] have been performed with this method. The method has also been used to compute the solidification of impure materials such as alloys [31,35]. The phase-field method is inherently a diffuse interface method [36], i.e. although the phase-field evolution equations reduce asymptotically to the sharp-interface ones with decreasing interface thickness, in practical implementation, the solid–liquid interface is spread over a region occupying a few mesh points. On the other hand, while the immersed boundary method [37], applied to the dendritic growth problem by Juric and Tryggvasson [1], tracks the interface as a sharp entity over an Eulerian grid, the interaction of the interface with the underlying mesh is accomplished through a numerical delta function which redistributes singular sources (latent heat) and jumps (material properties) onto the underlying mesh. Similar to the immersed interface method [2], no smearing of the interface results in the present method. It is found in the calculations presented herein that the solute boundary layers are extremely thin. Thus, unless very fine meshes are used, spreading of the interface over even a few mesh cells can lead the diffuse interface to occupy a region comparable in extent to the solute boundary layer thickness. Thus, a sharp treatment of the interface is highly desirable in calculating the solidification of impure materials. There has been some previous work in applying sharp-interface numerical approaches to the solution of the solidification problem for impure materials [38]. However, these utilized moving grid formulations, which are required to deal with issues of mesh quality, redefinition etc. when the interfaces become highly convoluted. To the authors' knowledge, this is the first attempt at devising a sharp-interface Eulerian methodology for the simulation of solidification in impure materials.

2. Formulation

The thermal and solutal transport in the solid and liquid phases are diffusion-driven and the following transport equations are solved in each phase:

$$\frac{\partial T}{\partial t} = \alpha_{\mathrm{l/s}} \nabla^2 T \tag{1}$$

$$\frac{\partial C}{\partial t} = D_{\mathrm{l/s}} \nabla^2 C \tag{2}$$

where T is the temperature, C is the solute concentration, α is the thermal and D is the solutal diffusivity. Subscripts s and l denote the solid and liquid phases respectively. These equations are solved with appropriate boundary conditions at the edges of the computational domain as well as with the following conditions at the advancing solidification front.

The Stefan condition provides conservation of heat at the interface:

$$\rho_{\mathrm{l}} L V_{\mathrm{N}} = k_{\mathrm{s}} \left(\frac{\partial T}{\partial n} \right)_{\mathrm{s}} - k_{\mathrm{l}} \left(\frac{\partial T}{\partial n} \right)_{\mathrm{l}} \tag{3}$$

where ρ_{l} is the density of the liquid, L is the latent heat of fusion, V_{N} is the normal velocity of the front and k_{s} and k_{l} are the thermal conductivities in the solid and liquid phases respectively. The derivatives of the temperature in the direction normal to the interface are

implied above. Solute conservation at the interface is given by Kurz and Fisher [39]:

$$(1-k_{\mathrm{p}})C_{\mathrm{l,int}}V_{\mathrm{N}} = D_{\mathrm{s}}\left(\frac{\partial C}{\partial n}\right)_{\mathrm{s}} - D_{\mathrm{l}}\left(\frac{\partial C}{\partial n}\right)_{\mathrm{l}} \tag{4}$$

k_{p} is the solute partition coefficient. The interface temperature and interface species concentration in the liquid phase are related through the phase diagram (the liquidus curve) and the capillarity effect. This relationship is given by [40]:

$$T_{\mathrm{l,int}} = b_0 + b_1 C_{\mathrm{l,int}} + b_2 C_{\mathrm{l,int}}^2 + b_3 C_{\mathrm{l,int}}^3 + b_4 C_{\mathrm{l,int}}^4 - \frac{\gamma_{\mathrm{sl}}(\theta)}{L} T_{\mathrm{m}}\kappa \tag{5}$$

where γ_{sl} is the solid–liquid interfacial tension, T_{m} is the equilibrium melting temperature and κ is the interface curvature. The values of the constants b_0–b_4 are given in Appendix A for the particular solution chosen here for the numerical calculations [22]. Note that the interfacial tension has a directional dependency, which imposes crystalline anisotropy. A model for such anisotropy [29] is included here, so that

$$\gamma_{\mathrm{sl}}(\theta) = \gamma_0(1 - 15\varepsilon\cos(m\theta)) \tag{6}$$

where θ is the angle with respect to the horizontal, the parameter ε regulates the anisotropy strength and m the symmetry characteristics (i.e. $m = 4$ for fourfold symmetry and $m = 6$ for sixfold cases computed later in this paper). The equations are non-dimensionalized by choosing the following scales: length scale $= X$, a characteristic length for the system, time scale $= X^2/D_{\mathrm{l}}$, concentration scale $= c_0$, the initial solute concentration, temperature scale $= T_{\mathrm{m}}$, the equilibrium melting temperature. The non-dimensional temperature is defined to be $\Theta = (T - b_0)/T_{\mathrm{m}}$ and non-dimensional concentration $c = C/C_0$, where C_0 is the concentration of salt in the initial solution. The non-dimensionalized equations are then written, as

$$\text{Energy equation:}\ \frac{\partial\Theta}{\partial t} = Le_{\mathrm{l/s}}\nabla^2\Theta \tag{7}$$

where Le is the Lewis number, $Le_{\mathrm{l/s}} = \alpha_{\mathrm{l/s}}/D_{\mathrm{l}}$.

$$\text{Species equation:}\ \frac{\partial c_{\mathrm{s}}}{\partial t} = \frac{D_{\mathrm{s}}}{D_{\mathrm{l}}}\nabla^2 c_{\mathrm{s}} \tag{8}$$

in the solid and

$$\frac{\partial c_{\mathrm{l}}}{\partial t} = \nabla^2 c_{\mathrm{l}} \tag{9}$$

in the liquid. The interface conditions become, in non-dimensional form:

$$V_{\mathrm{N}} = \frac{k_{\mathrm{l}}T_{\mathrm{m}}}{LD_{\mathrm{l}}}\left[\frac{k_{\mathrm{s}}}{k_{\mathrm{l}}}\left(\frac{\partial\Theta}{\partial n}\right)_{\mathrm{s}} - \left(\frac{\partial\Theta}{\partial n}\right)_{\mathrm{l}}\right] \tag{10}$$

We define a Stefan number, $St = k_{\mathrm{l}}T_{\mathrm{m}}/LD_{\mathrm{l}} = 563.673$ for the values chosen (see Appendix A).

$$V_{\mathrm{N}} = \frac{1}{(1-k)c_{\mathrm{l,int}}}\left[\frac{D_{\mathrm{s}}}{D_{\mathrm{l}}}\left(\frac{\partial c}{\partial n}\right)_{\mathrm{s}} - \left(\frac{\partial c}{\partial n}\right)_{\mathrm{l}}\right] \tag{11}$$

and

$$\Theta_{\mathrm{l,int}} = \frac{b_1 c_0}{T_{\mathrm{m}}}c_{\mathrm{l,int}} + \frac{b_2 c_0^2}{T_{\mathrm{m}}}c_{\mathrm{l,int}}^2 + \frac{b_3 c_0^3}{T_{\mathrm{m}}}c_{\mathrm{l,int}}^3 + \frac{b_4 c_0^4}{T_{\mathrm{m}}}c_{\mathrm{l,int}}^4 - \Gamma(\theta)\kappa \tag{12}$$

3. The numerical method

3.1. Discrete form of the governing equations

The present method computes temperature and solute field on a fixed Cartesian mesh, while the solid–liquid front evolves through the mesh. The interface is tracked using markers connected by piecewise quadratic curves parametrized by the arclength [5]. In Ye et al. [7] we provided details regarding the interaction of the interfaces with the underlying fixed Cartesian mesh. These include obtaining locations where the interface cuts the mesh, identifying phases in which the cell-centers lie, and procedures for obtaining a consistent mosaic of control volumes in the cells crossed by the immersed interface. This results in the formation of control volumes near the interface that are, in general, trapezoidal in shape (see Fig. 2). A finite-volume discretization is then performed over the regular Cartesian grid cells in the bulk of the computational domain and a lower-dimensional set of irregularly shaped cells that adjoin the interface.

The energy equation, Eq. (7), is written in semi-discrete form as (note that the symbols here represent non-dimensional quantities):

$$\int_v \frac{\Theta^{n+1} - \Theta^n}{\delta t}\,\mathrm{d}V = \frac{Le_i}{2}\oint(\nabla\Theta^{n+1} + \nabla\Theta^n)\hat{n}\,\mathrm{d}S \tag{13}$$

The above Crank–Nicolson scheme provides nominal second-order temporal accuracy. Spatial and temporal discretization accuracy studies have been reported in Ye et al. [7] and Udaykumar et al. [6,8]. The details of the discretization scheme are also provided in those papers and are only adumbrated here.

In discrete form Eq. (13) is written, for a control volume in the Cartesian mesh indexed (i, j) as

$$\frac{\Delta V_{ij}}{\delta t}(\Theta_{ij}^{n+1} - \Theta_{ij}^n) = \frac{Le_i}{2}\sum_{f=1}^{5}\left(\frac{\partial\Theta^{n+1}}{\partial n} + \frac{\partial\Theta^n}{\partial n}\right)_f \Delta S_f \tag{14}$$

In the above, n is the time level, ΔV_{ij} is the volume of the cell indexed i, j and ΔS_f is the area of the face of the control volume (see Fig. 2). In Eq. (14) above the

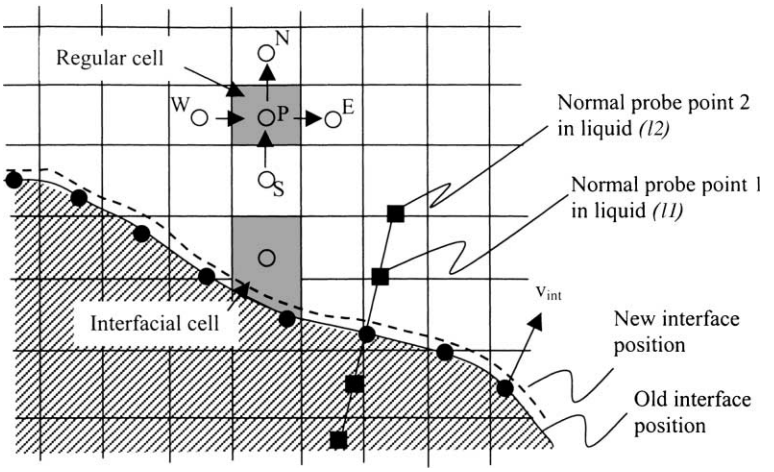

Fig. 2. Illustration of a moving boundary cutting through a fixed mesh. Cells traversed by the interface are called interfacial cells and are trapezoidal in shape. Cells away from the interface are regular cells. The normal probe to obtain interface velocity is also shown.

summation runs over the sides of the irregular-shaped (four- or five-sided) control volumes. The finite-volume discretization requires evaluation of the diffusive fluxes at the faces of each control volume, viz.:

$$F_{\mathrm{d}} = \nabla\Theta \cdot \vec{n} \tag{15}$$

For a uniform Cartesian mesh, the fluxes on the face-centers can be computed to second-order accuracy with a linear profile for the temperature field between neighboring cell-centers. This is not the case for a trapezoidal boundary cell since the center of some of the faces of such a cell may not lie halfway between neighboring cell-centers. These fluxes are obtained using a compact two-dimensional (2-D) polynomial interpolating function, described in Ye et al. [7], which allows us to obtain a second-order accurate approximation of the fluxes and gradients on the faces of the trapezoidal boundary cells from available neighboring cell-center values. This interpolation scheme coupled with the finite-volume formulation guarantees that the accuracy and conservation property of the underlying algorithm is retained even in the presence of arbitrary-shaped immersed boundaries. This has been demonstrated in Ye et al. [7] for stationary immersed boundaries and in Udaykumar et al. [8] for moving solid boundaries embedded in flows. In Udaykumar et al. [6] we showed that the solutions to the dendritic growth of pure materials from the melt are in agreement with microscopic solvability theory. The physically correct steady-state tip characteristics are selected when the dendrites are grown from seed crystals with arbitrary initial conditions.

In summary, the procedure for discretization above enables the formulation of fluxes using the general forms: gradients (for diffusive fluxes) at the non-interfacial sides of the control volume $F_f = \left(\sum_{l=1}^{6} \beta_l \Theta_l\right)_f$ and gradients (for diffusive fluxes) at the interfacial sides of the control volume $F_{\mathrm{int}} = \left(\sum_{l=1}^{9} \beta_l \Theta_l\right)_{\mathrm{int}}$.

In the above, subscript f stands for the face of the control volume (faces 1–4, Fig. 2), and subscript 'int' for the interfacial side (side 5, Fig. 2). Substitution of these expressions in the Eq. (14) results in a general discrete form:

$$\left(\frac{\Theta_{ij}^{n+1} - \Theta_{ij}^{n}}{\delta t}\right)\delta V_{ij} = Le_i \sum_{f=1}^{4} \frac{1}{2}\left[\left(\sum_{l=1}^{6} \beta_l \Theta_l^{n+1}\right)_f + \left(\sum_{l=1}^{6} \beta_l \Theta_l^{n}\right)_f\right] \mathrm{d}S_f + Le_i \left(\sum_{l=1}^{9} \beta_l \Theta_l\right)_{\mathrm{int}} \mathrm{d}S_{\mathrm{int}} \tag{16}$$

which can be written as

$$\sum_{l=1}^{l_{\max}} a_l \Theta_l^{n+1} = S(\Theta^n, \Theta_{\mathrm{int}}^{n+1}) \tag{17}$$

where the explicit terms, boundary and interface contributions and the accompanying interpolation coefficients are absorbed in the source term $S(\cdot)$. The summation runs over all the $l_{\max}$ computational points that are included in the stencils for the cell-face flux evaluations. The current computational point (i, j) is of course also included in the $l_{\max}$ stencil points. In cells away from the interface, as usual $l_{\max} = 5$, while for the interfacial cells, $5 \leqslant l_{\max} \leqslant 9$, and depends on the interface orientation and shape of the irregular cell [7,8]. Eq. (17) is solved using a standard line-SOR procedure, with alternate sweeps in the i- and j-directions with the

Thomas algorithm for the solution of the resulting tri-diagonal matrix. The use of a regular Cartesian grid allows for the use of these fast solution procedures.

The discretization of the solute diffusion equation in the liquid and solid phases is performed in a manner identical to that of the temperature field. Finally, since the inside of the immersed boundary is treated in the same manner as the outside, it is a straightforward matter to entertain arbitrarily large jumps in transport properties (without smoothing them) across the phase boundary or even to solve a different set of equations inside the immersed boundary. In this paper, we will use this feature to compute the diffusion of heat and solute with discontinuities in transport coefficients across the solid–liquid interface.

3.2. Application of interfacial conditions

In the case of solidification of pure materials, the application of the interfacial conditions is relatively straightforward, since the interface temperature is given by the Gibbs–Thompson condition and the interface velocity is computed using the Stefan condition [6]. An implicit scheme for the calculation of interface temperature and position is necessary to perform the computations with reasonable time step sizes. Such a coupled procedure is described in Udaykumar et al. [5]. In the present case, the interfacial temperature, composition, and velocity are coupled through the three equations (10)–(12). All three must be simultaneously satisfied for the case in which latent heat is not to be ignored. Note that in the isothermal case, where the spatial distribution of the temperature is uniform in the sample, only Eqs. (11) and (12) are required, since the interface temperature will be known a priori. In that case, the equation set to be solved is no different from the pure material case except that the solute concentration takes the place of temperature. Such an isothermal setting is closely approximated in cryobiology experiments on microscopic samples of cell suspensions performed using laboratory cryomicroscopy [9,19], but may not be applicable in freezing of tissue components.

In the present general treatment of coupled heat and solute transport, several approaches for applying the interface conditions were explored and the following method was deemed to be most suitable, within the framework of an implicit interface update.

3.2.1. Interface velocity

The interface velocity is computed using Eq. (4). The required concentration gradients in the liquid and solid phases are computed using the normal probe technique described in Udaykumar et al. [5]. We briefly describe the procedure with the aid of Fig. 2. The values of solute concentration at the nodes of the normal probe, spaced at equal distances $\mathrm{d}x$ (the mesh spacing) along the probe, are determined by bilinear averaging from the surrounding computational points. Thus, the gradients in the liquid phases are evaluated from:

$$\left(\frac{\partial c}{\partial n}\right)_{\mathrm{l}} = \frac{4c_{\mathrm{l1}} - c_{\mathrm{l2}} - 3c_{\mathrm{l,int}}}{2\,\delta x} \tag{18}$$

where subscripts l1 and l2 imply evaluations of concentration at the two nodes on the normal probe and subscript int implies the value on the interface. Similar evaluation of concentration gradient is performed in the solid phase. Having calculated the concentration gradients in each phase using Eq. (18), the interface velocities are computed at the markers using Eq. (11).

3.2.2. Interface temperature

Once the velocity is computed, the interface temperature is obtained using Eq. (10). Thus, in the following interface condition:

$$V_{\mathrm{N}} = St\left[\frac{k_{\mathrm{s}}}{k_{\mathrm{l}}}\left(\frac{\partial \Theta}{\partial n}\right)_{\mathrm{s}} - \left(\frac{\partial \Theta}{\partial n}\right)_{\mathrm{l}}\right] \tag{19}$$

V_{N} is treated as known and the interface temperature is computed, with $\Theta_{\mathrm{l,int}} = \Theta_{\mathrm{s,int}}$. To calculate the temperature gradient at the interface $\partial\Theta/\partial n$ with an $\mathrm{O}(\mathrm{d}x^2)$ error, we use the values of temperature at two points along the normal probe.

In the liquid, the temperature values at the two points along the normal probe are denoted Θ_{l1} and Θ_{l2} respectively, and are obtained by bilinear interpolation from the surrounding grid nodes. Let the distance of these two points on the normal probe be $\mathrm{d}x_{\mathrm{l1}}$ ($= \mathrm{d}x$, the grid size) and $\mathrm{d}x_{\mathrm{l2}}$ ($= 2\,\mathrm{d}x$) respectively from the interfacial marker where the temperature is to be computed. A Taylor series expansion about the interfacial point gives

$$\Theta_{\mathrm{l1}} = \Theta_{\mathrm{l,int}} + \left(\frac{\partial \Theta}{\partial n}\right)_{\mathrm{l}} \mathrm{d}x_{\mathrm{l1}} + \left(\frac{\partial^2 \Theta}{\partial n^2}\right)_{\mathrm{l}} \frac{(\mathrm{d}x_{\mathrm{l1}})^2}{2!} + \mathrm{O}\left(\mathrm{d}x_{\mathrm{l1}}^3\right) \tag{20}$$

$$\Theta_{\mathrm{l2}} = \Theta_{\mathrm{l,int}} + \left(\frac{\partial \Theta}{\partial n}\right)_{\mathrm{l}} \mathrm{d}x_{\mathrm{l2}} + \left(\frac{\partial^2 \Theta}{\partial n^2}\right)_{\mathrm{l}} \frac{(\mathrm{d}x_{\mathrm{l2}})^2}{2!} + \mathrm{O}\left(\mathrm{d}x_{\mathrm{l2}}^3\right) \tag{21}$$

From the above equations, we get the second-order approximation:

$$\left(\frac{\partial \Theta}{\partial n}\right)_{\mathrm{l}} = \frac{\mathrm{d}x_{\mathrm{l2}}^2\Theta_{\mathrm{l1}} - \mathrm{d}x_{\mathrm{l1}}^2\Theta_{\mathrm{l2}} - \left(\mathrm{d}x_{\mathrm{l2}}^2 - \mathrm{d}x_{\mathrm{l1}}^2\right)\Theta_{\mathrm{l,int}}}{\mathrm{d}x_{\mathrm{l1}}\mathrm{d}x_{\mathrm{l2}}^2 - \mathrm{d}x_{\mathrm{l1}}^2\mathrm{d}x_{\mathrm{l2}}} \tag{22}$$

which may be written as

$$\left(\frac{\partial \Theta}{\partial n}\right)_{\mathrm{l}} = a_{\mathrm{l1}}\Theta_{\mathrm{l1}} + a_{\mathrm{l2}}\Theta_{\mathrm{l2}} + a_{\mathrm{li}}\Theta_{\mathrm{l,int}} \tag{23}$$

The gradient in the solid can be similarly obtained.

Thus, Eq. (19) becomes, with the fact that $\Theta_{l,int} = \Theta_{s,int}$, i.e. continuity of temperature at the interface:

$$V_N = St\left[\frac{k_s}{k_l}(a_{s1}\Theta_{s1} + a_{s2}\Theta_{s2} + a_{s,int}\Theta_{l,int}) - (a_{l1}\Theta_{l1} + a_{l2}\Theta_{l2} + a_{l,int}\Theta_{l,int})\right] \quad (24)$$

Since the interface velocity has been determined from Eq. (11) above, inversion of Eq. (24) provides the interface temperature:

$$\Theta_{l,int} = \frac{\frac{V_N}{St} - \frac{k_s}{k_l}(a_{s1}\Theta_{s1} + a_{s2}\Theta_{s2}) + (a_{l1}\Theta_{l1} + a_{l2}\Theta_{l2})}{\frac{k_s}{k_l}a_{s,int} - a_{l,int}} \quad (25)$$

3.2.3. Interface composition

Next, the interface composition on the liquid side of the interface is obtained from Eq. (12), using the above determined value of the interface temperature. The nonlinear equation for c_{Li} is solved using a Newton method using

$$b_1 c_{l,int} + b_2 c_{l,int}^2 + b_3 c_{l,int}^3 + b_4 c_{l,int}^4 = \Theta_{l,int} + \frac{\gamma_{sl}(\theta)}{L}\Theta_m \kappa \quad (26)$$

The composition on the solid side is then given by the partition coefficient:

$$c_{s,int} = k_p c_{l,int} \quad (27)$$

Once the interface values are obtained, the interfacial markers are advected to new positions in order to evolve the interface in time. Once the interface has moved to its new position, the interface markers are redistributed at uniform arclength spacing $ds = O(dx)$, where dx is the local grid spacing. Points are added or deleted on the interface as necessary to maintain adequate interface resolution. The normal and curvature at the interfacial markers are computed as described in Udaykumar et al. [5]. The curvature κ and orientation θ $(= \tan^{-1}(n_y/n_x))$ are then used in applying the boundary condition, via Eq. (12) in solving the governing equations in the next iteration.

3.3. Overall solution procedure

For curvature-driven growth problems, stability of the interface update requires an implicit coupled procedure for obtaining the field solution [33,41] and the interface position simultaneously at time level t^{n+1}. In the absence of such an implicit, coupled treatment of the field solution and interface evolution, the calculations can become very stiff. The stability restriction on an explicit scheme can be very severe ($\delta t = O(dx^3)$) as demonstrated by Hou et al. [33].

Furthermore, as described in Section 3.2, the interfacial conditions in the present case couple the interface position (and curvature), temperature and composition. An implicit procedure similar to that employed in Udaykumar et al. [5] is used in the present work. The overall solution procedure with boundary motion is as follows:

1. Advance to time $t = t + \delta t$. Iteration counter $k = 0$.
2. Augment iteration counter, $k = k + 1$.
3. Determine the intersection of the immersed boundary with the Cartesian mesh.
4. Using this information, reshape the boundary cells.
5. For each reshaped boundary cell, compute and store the coefficients appearing in discrete form, Eq. (17).
6. Get $\Theta_{l,int}$ from V_N using Eq. (25).
7. Get $c_{l,int}$ from $\Theta_{l,int}$ using Eq. (26).
8. Advance the discretized equations in time. Compute the temperature and composition fields using the boundary conditions in steps 6 and 7 above.
9. Get V_N using Eq. (11). Advance the interface position in time.
10. Check whether the temperature field and interface have converged. Convergence is declared if $\max|T_{ij}^k - T_{ij}^{k-1}| < \varepsilon_T$, $\max|c_{ij}^k - c_{ij}^{k-1}| < \varepsilon_c$ and $\max|X_{int}^k - X_{int}^{k-1}| < \varepsilon_I$ where k is the iteration number and ϵ's are convergence tolerances set in each case to 10^{-5} in the calculations so that the solution obtained is independent of the convergence criterion.
11. If not converged, go to step 2 for next iteration. If converged, go to step 1 for next time step.

Typically, after the initial transients have settled, less than five iterations are required for convergence since the previous time step solution provides an excellent guess to the solution at the current step. Note that with this implicit iterative approach stable computations of interface evolution can be performed with time step sizes that are controlled by a CFL-type criterion of the form $\delta t = \lambda \delta x / \max(V_{Interface})$, where λ is set to 0.1 in the calculations performed.

4. Results

4.1. Planar (1-D) calculations

We first compute the evolution of a planar solidification front under the boundary conditions described above. This 1-D case was solved using a coordinate system fixed at the advancing front by Wollhover et al. [23]. They obtained numerical (finite-difference) solutions for the temperature and solute fields ahead of the front. We have computed the cases in Wollhover et al. and find good agreement with their results. A schematic of the setup for the 1-D calculations is shown in Fig. 3(a).

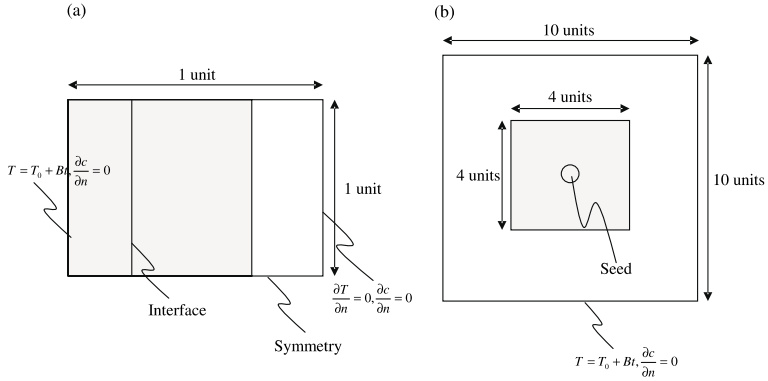

Fig. 3. Schematic of computational setup for (a)1-D and (b) 2-D solidification calculations. The fine mesh region and the boundary conditions are shown.

The temperature at the left wall (at the boundary of the solid) is decreased in time at a constant specified cooling rate. The range of cooling rates investigated in the following is typical of the rates employed in cryoprotocols. The right wall is treated as an adiabatic boundary. The solid–liquid front then advances in the $+x$ direction.

Two typical cases are shown in Figs. 4 and 5. The cooling rate in Fig. 4 is $B = -0.05$. This is the lowest cooling rate computed. Fig. 4(a) shows the temperature field at various instants of time as the front advances to the right. As can be seen, at this low cooling rate, the temperature field has only mild variations in space due to the large thermal diffusivity. However, the solute is segregated into the solution as the ice forms and a solute boundary layer progressively accumulates ahead of the front. The solute layer steepens as time progresses since almost pure ice forms upon solidification. For this growth configuration there is a region of constitutionally supercooled solution in front of the ice–liquid boundary as shown in Fig. 4(c). The constitutional supercooling was computed as the difference between the equilibrium freezing temperature obtained from the local composition via Eq. (12), and the actual temperature at that

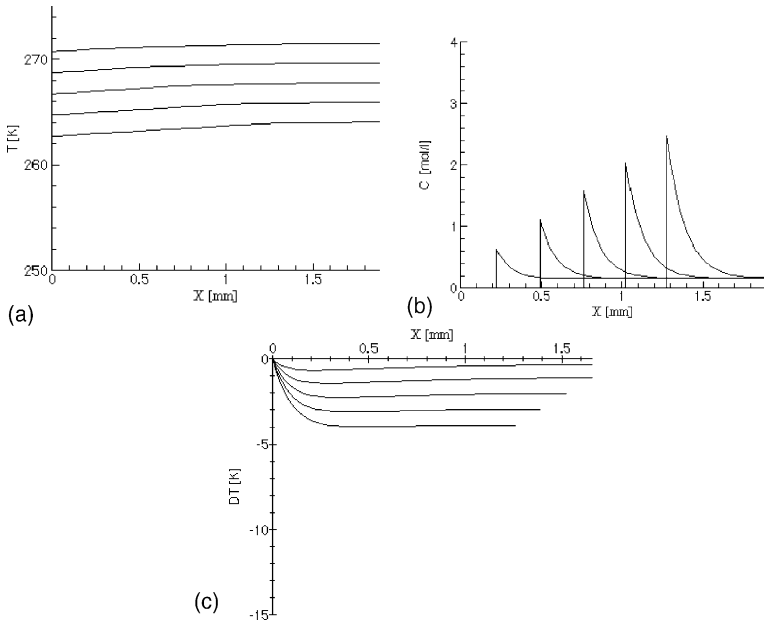

Fig. 4. 1-D solidification calculations of an aqueous solution for a cool rate of $B = -0.05$ K/s. (a) Temperature field in the liquid and solid phases at time intervals of 40 s. The time instants are numbered in sequence. (b) Species concentration in the solid and liquid phases. (c) Constitutional supercooling in the liquid phase ahead of the front.

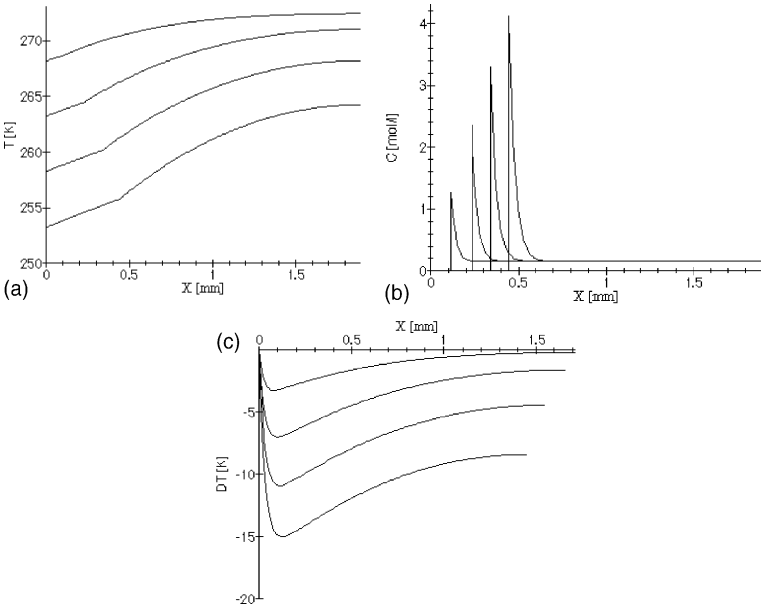

Fig. 5. 1-D solidification calculations of an aqueous solution for a cool rate of $B = -1.0$ K/s. (a) Temperature field in the liquid and solid phases at time intervals of 5 s. The time instants are numbered in sequence. (b) Species concentration in the solid and liquid phases. (c) Constitutional supercooling in the liquid phase ahead of the front.

point. The results shown in Fig. 4(a)–(c) are in excellent agreement (see Fig. 6 for a quantitative comparison) with those in Wollhover et al. [23]. It is to be noted that the present sharp-interface method captures the solute buildup on the liquid side of the interface as a discontinuity and also treats the diffusivity jump between the solid and liquid as a jump discontinuity. Thus, in the calculations performed here, the salt is rejected into the remaining solution entirely while nearly pure solid (ice) forms.

In Fig. 5, we show the results for planar front propagation for the largest cooling rate calculated, i.e. $B = -1.0$, a cooling rate 20 times higher than in the previous case. For this large cooling rate, the temperature field in the solid and liquid display very different gradients, even though the thermal diffusivity is large. The discontinuity in the slope of the temperature profile at the interface is clearly seen. The velocity of the interface computed from Eq. (11) is therefore very high for this case. This leads to a very steep solute boundary layer in front of the solid–liquid boundary. There is also a progressively deepening region of constitutionally supercooled liquid ahead of the ice front. The front under such circumstances would be expected to become unstable via the Mullins–Sekerka mechanism and therefore the ice front will typically advance in a cellular/dendritic manner as observed by Koerber et al. [22].

The interface location for various cooling rates is plotted against time in Fig. 6(a). These curves were produced to compare with identical curves in Wollhover et al. [23]. In Fig. 6(a), the solid lines are curves obtained by the present method, while the dotted lines are those in Wollhover et al. There is close agreement between the results. We have also established that the results presented in the figure are grid independent. In Fig. 6(b) we show the interface temperature and in Fig. 6(c) the interface species concentrations in time as the solidification front advances. The results for three different mesh spacings (40, 80 and 120 mesh points respectively) are shown in the figures. Unlike Wollhover et al., who use initial conditions that are a continuation of semi-analytical results, the initial conditions are somewhat arbitrary in our case (a uniform concentration field corresponding to the initial solution concentrations is specified and the interface temperature is taken to be the equilibrium value). The initial transients appear to displace the coarsest mesh solution somewhat far from the two finer mesh cases. The two fine mesh solutions are almost indistinguishable from each other, unless amplified as in the inset. Furthermore, for the coarsest mesh, the crossing of the interface across the mesh points gives rise to small periodic excursions in the interface temperature value, while for the finer meshes the solution progresses smoothly.

4.2. Two-dimensional calculations

The dendritic growth of crystals coupled with the transport of heat and solute was computed for a range of physical parameters. The cases were designed to

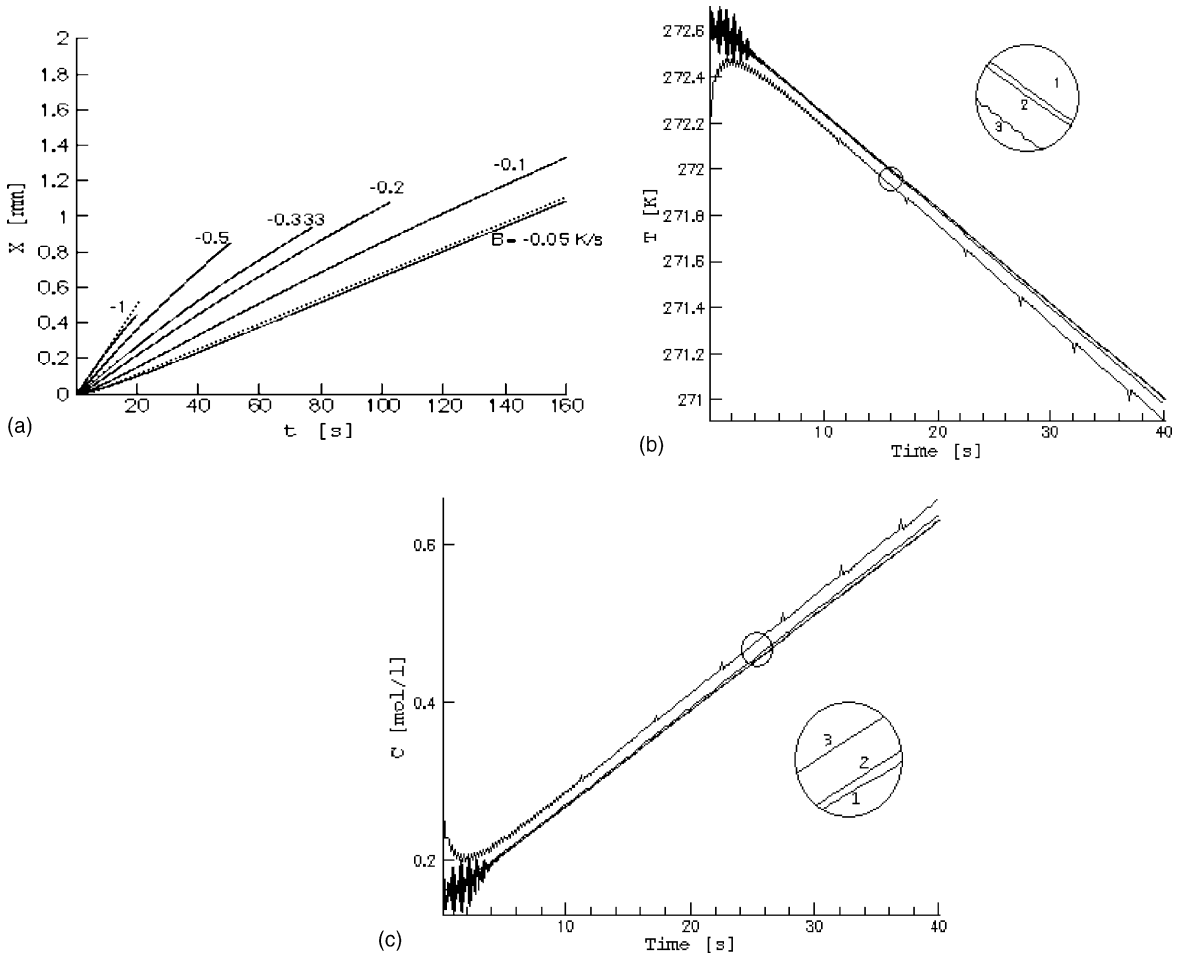

Fig. 6. Test of accuracy of the 1-D computations. (a) Plot of interface position against time. The solid line is the trajectory computed from the present calculation. The dotted line is the result from Koerber et al. (b) Time variation of the interface temperature for the cooling rate value of $B = -1.0$ K/s. The finest grid is labeled 1 and the coarsest grid is labeled 3. (c) The interface concentration computed for the three meshes for the case of $B = -1.0$ K/s.

demonstrate the capability of the present sharp-interface technique to compute the large distortions of the phase boundary, while maintaining explicit information on the interface shape and discontinuities in the material properties and solute fields across the boundary. This method was shown in Udaykumar et al. [8] to compute the pure material dendritic growth accurately and to agree with theoretical predictions, based on microscopic solvability theory [40]. Here we show that the results display the correct physically expected trends as the growth parameters are varied.

A schematic of the computational setup is shown in Fig. 3(b). Typical theoretical treatment, approximating some experimental protocols of the freezing process in the cryopreserving solutions, assume that the temperature is spatially uniform but temporally varying [10, 14,16,18], the so-called isothermal model. We include heat transport, in order to make the simulations completely general and because in reality, thermal gradients are unavoidable in the putative isothermal experiments unless the latent heat is removed very rapidly, and thermal gradients are inherent in directional solidification experiments in cryotreatment [19]. Thus, the isothermal model can be treated as a special case of the calculations to be performed here. This requires the full coupling of the interface temperature, composition and velocity through the interface conditions, Eqs. (10)–(12). The Stefan number is very large in the following simulations ($St = 563.673$), thus rendering the temperature gradients shallow in the domain as will be shown in results later. Furthermore, the thermal diffusivity being much larger than species diffusivity, diffusional solute transport away from the interface controls the progress of the solidification front. In the calculations presented, the tempera-

ture at the edges of the computational domain is varied in time according to the required cooling rate. The species gradients are set to zero at the edges. Thus

$$\Theta(x_{\partial\Omega}, y_{\partial\Omega}, t) = \Theta_0 + Bt \tag{28}$$

$$\frac{\partial}{\partial n} c(x_{\partial\Omega}, y_{\partial\Omega}, t) = 0 \tag{29}$$

where B is the cooling rate and subscript $\partial\Omega$ indicates points on the edges of the domain. The initial conditions for these cases were specified as follows:

$$\Theta(x, y, 0) = \Theta_0, \quad c_l(x, y, t) = c_0, \quad c_s(x, y, t) = k_p c_0$$

In Fig. 7 we show the development of the interface for a case with sixfold anisotropy. The domain size is 10×10 units and the fine grid region occupies the region between $x = 3$–7 and $y = 3$–7. The number of grid points in each direction in the fine grid region is 500, thus $dx = 0.008$. The cool rate imposed on the edge is $B = -0.1$. Other parameters specified are $\Gamma = 10^{-4}$, a non-dimensional value appropriate for water as the freezing material, and $\varepsilon = 0.05$. An initially placed small circular seed is allowed to grow and the development of the unstable front is shown at different instants of time in Fig. 7(a). The circular seed develops perturbations in

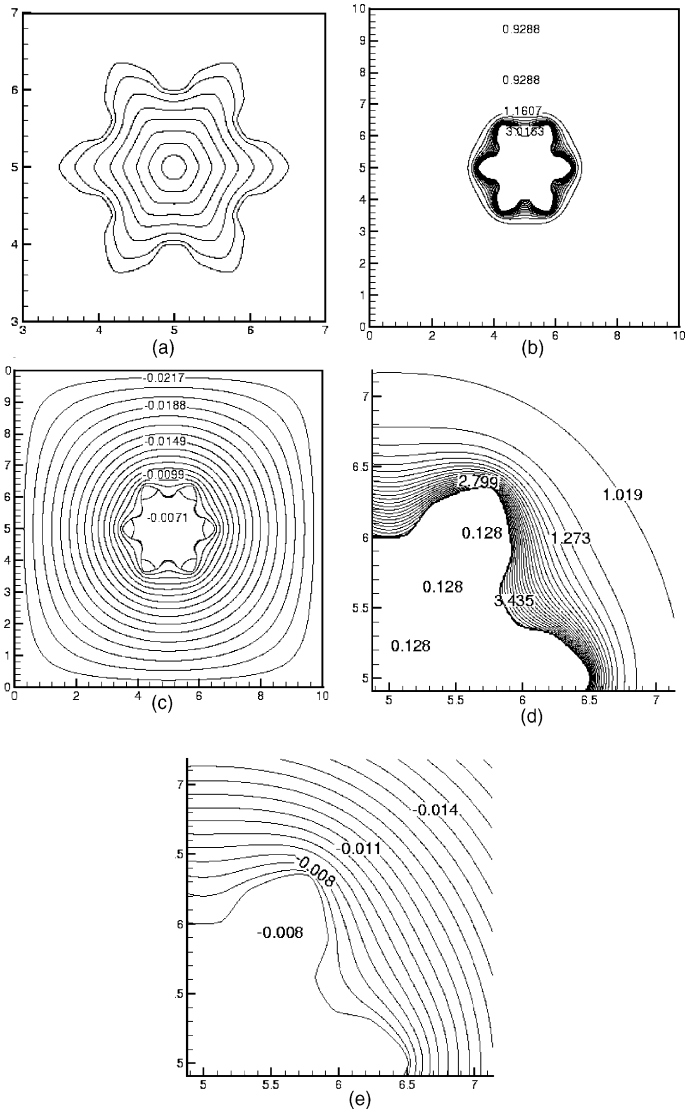

Fig. 7. Growth of a sixfold symmetric crystal from a circular seed. The capillary parameter $\Gamma =$, anisotropy strength = 0.5, cooling rate $B = -0.1$. (a) Shapes of the crystal at various time instants, (b) species concentration in the computational domain, (c) temperature contours in the domain, (d) close-up of species concentrations around the crystal and (e) close-up of the temperature field around the crystal.

the initial stage of the growth to form a hexagonal morphology aligned with the preferred growth directions. These perturbations then grow into primary dendritic branches. The solute progressively accumulates in the grooves between the branches. This microsegregation within the thin solute boundary layer is shown in Fig. 7(b). The temperature field is shown in Fig. 7(c) at the same instant in the growth as in Fig. 7(b). The thermal boundary layer is seen to be much wider than the solute boundary layer. In Fig. 7(d) and (e), we show close-up views of the solutal and thermal fields near a branch of the growing crystal. The large gradients of solute and the comparatively higher gradients of the temperature field in the vicinity of the growing tip are clearly seen in these figures. Also, the values of the contours indicated show that the solute accumulation in the grooves is higher than at the tip of the dendrite. Thus, in terms of the effect on cryopreservation, the cells that find themselves in the grooves between dendritic arms will experience more hypertonic environments relative to those that find themselves near the tip of the dendrite. Furthermore, Fig. 7(a) shows that the grooves are nearly stationary in the later stages of the growth of the crystal, while the tip grows rapidly. Thus, cells that are located near the grooves are likely to find themselves in a pool rich in salt for longer durations than those that are approached and engulfed by the tip. These facts impact significantly on the survival of the cells, as shown experimentally by cryobiological experiments [11,42] and indicate the importance of obtaining the temporal and spatial distribution of solute in predicting the fates of cells in ice-cell interactions.

In Fig. 8 we compute the development of a fourfold symmetric crystal, other parameters remaining the same as in Fig. 7. Again, the growth proceeds from an initial circular seed crystal. The dendrite primary arms form with parabolic tips of high curvature. Fig. 8(b) and (c) show the solute concentration and temperature contours around the growing crystal. In Fig. 9(a) we show the development of a crystal with identical growth conditions to Fig. 8(a), except that the anisotropy in this case is lowered to $\varepsilon = 0.01$. Comparison of Figs. 8(a) and 9(a) indicates that when the crystals have grown to nearly the same overall size, the tip curvature for the high anisotropy crystal is much higher than for the low anisotropy crystal. Also the species and thermal boundary layers in the latter case are shallower than for the previous high anisotropy case. The tip velocities in the high anisotropy case are also higher than that of the low anisotropy case. This fact would have implications for cells in cryopre-

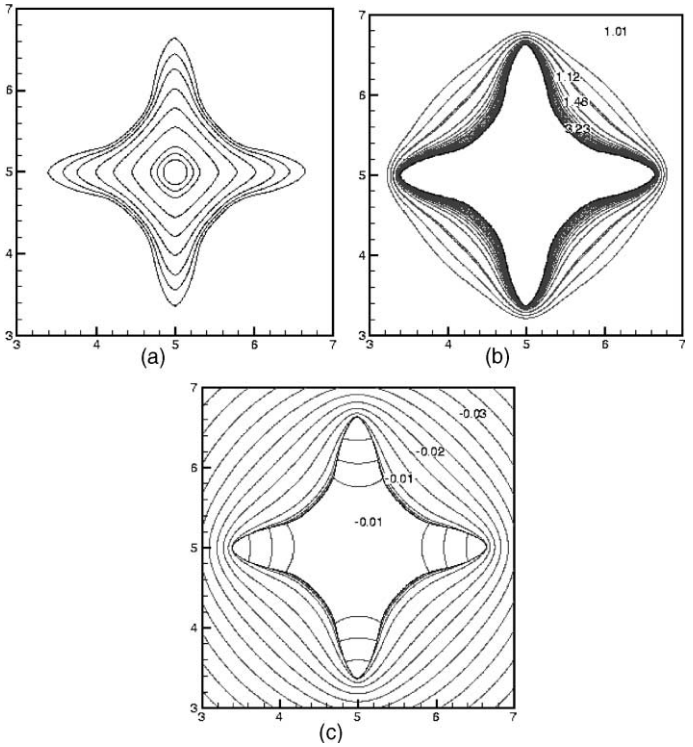

Fig. 8. Growth of fourfold symmetric crystal for the cooling rate of $B = -0.1$. The anisotropy strength $\varepsilon = 0.05$ (high value). (a) Crystal shapes are various times during the growth, (b) species concentrations around the crystal and (c) temperature field around the crystal.

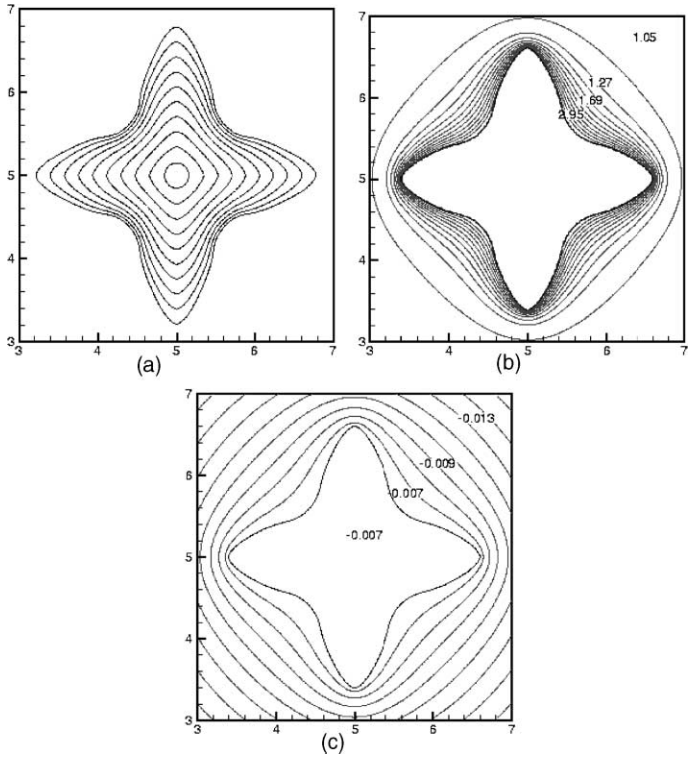

Fig. 9. Growth of fourfold symmetric crystal for the cooling rate of $B = -0.1$. The anisotropy strength $\varepsilon = 0.01$ (low value). (a) Crystal shapes are various times during the growth, (b) species concentrations around the crystal and (c) temperature field around the crystal.

servation, not only in terms of the compositional field and engulfment velocity experienced by the cell during its interaction with the ice, but also in mechanical interactions of the ice crystals with the cells [20,43].

In Fig. 10(a) and (b), we have considered the effect of the cooling rate on the growth of a fourfold symmetric crystal, whose growth axis has been rotated by 45° from the horizontal. We imposed this rotation of the growth direction to demonstrate that grid anisotropy does not impact negatively on the calculations. Such tests were previously performed for the pure dendrite cases in Udaykumar et al. [5]. The crystal grows with the expected fourfold symmetry without any traces of the grid-induced noise or anisotropy. In general, the manifestation of grid-induced effects is dependent on the growth conditions (supercooling, surface tension,

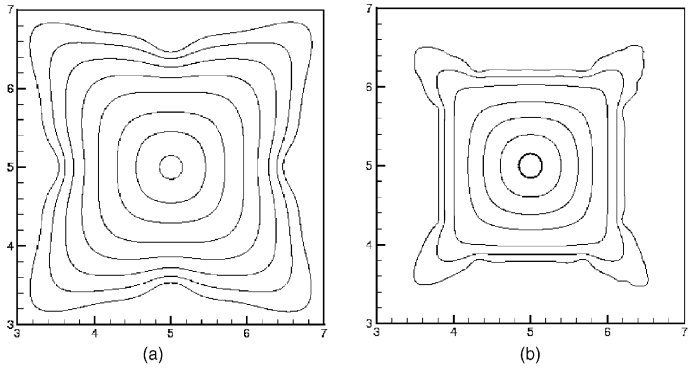

Fig. 10. Growth of fourfold symmetric crystal from the solution for a specified anisotropy strength of $\varepsilon = 0.01$: (a) for a low cooling rate of $B = -0.01$ and (b) for a high cooling rate of $B = -0.1$.

anisotropy value etc.). In contrast to Fig. 8, the anisotropy strength here is low, $\varepsilon = 0.01$. In Fig. 10(a), the cooling rate is the low value, i.e. $B = -0.01$. Here the crystal grows with fairly large tip radius. In Fig. 10(b), the cooling rate is the higher value, $B = -0.1$. The crystal assumes a more angular morphology in this case as compared to Fig. 10(a). In the final stages of growth the tip appears to show the development of instabilities that begin to assume the form of sidebranches. This behaviour and the noticeable asymmetry in this incipient breakdown is due to the lack of sufficient grid resolution to fully and accurately capture the tip dynamics in this stage. As observed previously [6], for dendrite tips that are driven to grow with higher velocities and smaller radii, the tip sensitivity to grid-induced noise is higher, and this tends to perturb the tip causing it to become sensitive and unstable to numerically generated perturbations. The sensitivity in Fig. 10(b) is exacerbated by the high cooling rate, which renders the tip sharper than that in Fig. 10(a) and thus less well resolved by the mesh provided. Real crystal tips of course are correspondingly sensitive to noise and generate sidebranches under sufficiently strong perturbation. It is possible to introduce controlled noise to initiate more regular side-branching events instead of relying on numerical noise [44], although the precise characteristics of ''real'' noise in experimental dendritic growth systems is difficult to estimate.

In Fig. 11 we show the long-time evolution of a dendritic crystal from the impure medium. The elongated domain of 2×10 units is shown in the figure. In this case symmetry conditions on both the temperature and solute fields were imposed on the left, right and bottom sides of the domain. At the top of the domain the temperature was specified based on the cool rate $B = -0.1$ and the zero-gradient condition was imposed on the species field. The growth of the crystal starting from the initial circular seed is shown in Fig. 11(a). The imposed fourfold symmetry ($\varepsilon = 0.05$) causes the crystal to grow rapidly in the preferred growth directions. However, as the thermal and solute boundary layers are confined by the symmetric sides of the domain, i.e. the latent heat and solute accumulate at the sides, only the arm of the crystal directed upward continues to grow freely. The tip of the crystal assumes a parabolic shape that subsequently becomes unstable and generates sidebranches, which in turn grow in the preferred horizontal direction. The sidebranches are again generated due to numerically induced noise and thus slight asymmetries in the final dendritic crystal are noticeable. The solute field surrounding the dendrite in the late stages is shown in Fig. 11(b). The very high concentrations in the grooves between the sidebranches may be noted. The bulk concentration value in the liquid is 1.30, the value at the tip of the dendritic arm is 4.53, while the concentration value in the first groove behind the tip is

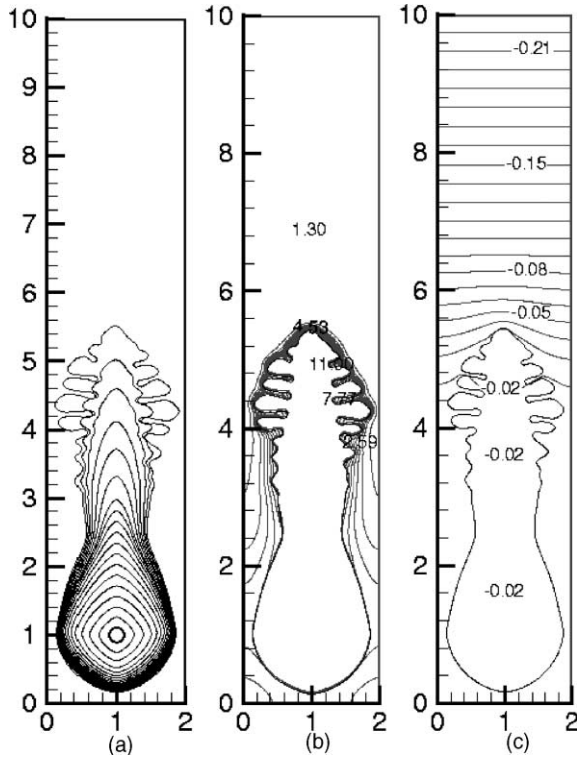

Fig. 11. Growth of fourfold symmetric crystal for the high cooling rate of $B = -0.1$. The anisotropy strength $\varepsilon = 0.05$ (high value). (a) Crystal shapes are various times during the growth, (b) species concentrations around the crystal and (c) temperature field around the crystal.

11.00. In Fig. 11(a) it can be seen that these solute-rich grooves once formed solidify only very slowly. The corresponding temperature field is shown in Fig. 11(c) and for the high Stefan number and thermal diffusivity used the thermal field displays only shallow gradients.

5. Summary

We have developed a numerical technique for tracking the evolution of freeze fronts in the presence of heat and solute transport at the microscale. The ice front is captured as a sharp solid–liquid interface in both the 1-D and planar cases. Our interest is in the computation of dendritic solidification of aqueous salt solutions used in cryopreservation of cells and tissue. In such systems the solute is rejected completely into the solution, with nearly pure ice formed as the solidification proceeds. We have compared our results with the simulations of Koerber and coworkers in the 1-D solidification case. However, we show that for the solidification conditions imposed in the 1-D test cases, the solute ahead of the

front is constitutionally supercooled. The planar front then suffers instability to assume cellular and dendritic forms. The present method has been shown to be capable of simulating the non-planar freezing of the solution. Although the primary goal of this paper was to present a numerical technique for capturing sharp interfaces in growth of impure materials (such as solutions and alloys), some preliminary insights into the physics of cyropreservation have been obtained. A cell that is immersed in such a medium during cryopreservation is exposed to an advancing ice front and the accompanying microsegregated solute boundary layer. This effect is typically ignored in simplified analytical studies of ice-cell interaction where the segregation of solute both at the cell boundary as well as the ice boundary is neglected and the medium is supposed homogeneous. However, the thermo-solutal environments experiences by cells in suspension in a salt solution are indeed inhomogeneous. Precise knowledge of the spatio-temporal variations of solutes and their interactions with cells will aid in better understanding, quantifying and predicting cell viability in freeze-thaw protocols. The application of the present method to the study of cell response to freezing is ongoing and is expected to advance quantitative analysis of cryopreservation effects on cells.

Acknowledgements

This work was supported in part by a National Science Foundation CAREER Award (CTS-0092750) and a Whitaker Foundation Biomedical Engineering Research Grant to Dr. H.S. Udaykumar.

Appendix A

The parameters employed in the calculations are the same as those of Koerber et al. [22]: concentration scale: $c_0 = 0.1548$ mol l^{-1}, thermal diffusivity of liquid: $\alpha_l = 0.115$ mm^2 s^{-1}, thermal diffusivity of solid: $\alpha_s = 1.364$ mm^2 s^{-1}, diffusivity of NaCl in liquid: $D_l = 7.8 \times 10^{-4}$ mm^2 s^{-1}, diffusivity of NaCl in solid: $D_s = 7.8 \times 10^{-7}$ mm^2 s^{-1}, latent heat of fusion: $L = 0.333$ J mm^{-3}, equilibrium freezing point: $T_m = 273.15$ K, partition coefficient: $k = (c_{Li})_s/(c_{Li})_l = 1.00 \times 10^{-3}$, thermal conductivity of liquid: $k_l = 5.36 \times 10^{-4}$ J mm^{-1} s^{-1} K^{-1}, thermal conductivity of solid: $k_s = 2.34 \times 10^{-3}$ J mm^{-1} s^{-1} K^{-1}.

Coefficients in the phase diagram:

$$T_{Li} = b_0 + b_1 c_{Li} + b_2 c_{Li}^2 + b_3 c_{Li}^3 + b_4 c_{Li}^4$$

$b_0 = 273.15$ K, $b_1 = -3.362$ K l mol^{-1}, $b_2 = -0.0414$ K l^2 mol^{-2}, $b_3 = -0.0404$ K l^3 mol^{-3}, $b_4 = -6.616 \times 10^{-4}$ K l^4 mol^{-4}.

References

[1] D. Juric, G. Tryggvasson, A front tracking method for dendritic solidification, J. Comput. Phys. 123 (1996) 127–148.
[2] R.J. Leveque, Z. Li, The immersed interface method for elliptic equations with discontinuous coefficients and singular sources, SIAM J. Numer. Anal. 31 (4) (1994) 1019–1044.
[3] F. Gibou, R.P. Fedkiw, L.-T. Cheng, M. Kang, A second-order-accurate symmetric discretization of the poisson equation on irregular domains, J. Comput. Phys. 176 (1) (2002) 205–227.
[4] T.Y. Hou, Z. Li, S. Osher, H. Zhao, A hybrid method for moving interface problems with application to the Hele–Shaw flow, J. Comput. Phys. 134 (2) (1997) 236–247.
[5] H.S. Udaykumar, R. Mittal, W. Shyy, Computation of solid–liquid phase fronts in the sharp interface limit on fixed grids, J. Comput. Phys. 153 (1999) 535–574.
[6] H.S. Udaykumar, R. Mittal, P. Rampunggoon, Interface tracking finite volume method for complex solid–fluid interactions on fixed meshes, Commun. Numer. Meth. Eng. 18 (2002) 89–97.
[7] T. Ye, R. Mittal, H.S. Udaykumar, W. Shyy, A Cartesian grid method for simulation of viscous incompressible flows with complex immersed boundaries, J. Comput. Phys. 156 (2) (1999) 209–240.
[8] H.S. Udaykumar, R. Mittal, P. Rampunggoon, A. Khanna, An Eulerian–Lagrangian Cartesian grid method for simulating flows with complex moving boundaries, J. Comput. Phys. 174 (2001) 1–36.
[9] B. Rubinsky, Microscale heat transfer in biological systems at low temperatures, Exp. Heat Transfer 10 (1997) 1–29.
[10] P. Mazur, Kinetics of water loss from cells at subzero temperatures and the likelihood of intracellular freezing, J. Gen. Physiol. 47 (1963) 347–369.
[11] P. Mazur, W.F. Rall, N. Rigopoulos, The relative contributions of the fraction of unfrozen water and of salt concentration to the survival of slowly frozen human erythrocytes, Biophys. J. 36 (1981) 653–675.
[12] M. Toner, E.G. Cravalho, M. Karel, Thermodynamics and kinetics of intracellular ice formation during freezing of biological cells, J. Appl. Phys. 67 (3) (1990) 1582–1593.
[13] A. Katchalsky, P.F. Curran, Nonequilibrium Thermodynamics in Biophysics, Harvard University Press, Cambridge, MA, 1981.
[14] P. Mazur, The role of intracellular freezing in the death of cells cooled at supra-optimal rates, Cryobiology 14 (1977) 251–272.
[15] M. Toner, E.G. Cravalho, M. Karel, Cellular response of mouse oocytes to freezing stress: prediction of intracellular ice formation, J. Biomech. Eng. 115 (1993) 169–174.
[16] J.O.M. Karlsson, E.G. Cravalho, M. Toner, Model of diffusion-limited ice growth inside biological cells during freezing, J. Appl. Phys. 75 (9) (1994) 4442–4455.
[17] W.W. Mullins, R.F. Sekerka, Stability of a planar interface during solidification of a dilute binary alloy, J. Appl. Phys. 35 (2) (1964) 444–451.
[18] J.O.M. Karlsson, A. Eroglu, T.L. Toth, E.G. Cravalho, M. Toner, Fertilization and development of mouse oocytes

cryopreserved using a theoretically optimized protocol, Human Reprod. 11 (6) (1996) 1296–1305.
[19] B. Rubinsky, M. Ikeda, A cryomicroscope using directional solidification for the controlled freezing of biological material, Cryobiology 22 (1985) 55–68.
[20] H. Takamatsu, B. Rubinsky, Viability of deformed cells, Cryobiology 39 (1999) 243–251.
[21] S. Kourosh, M.G. Crawford, K.R. Diller, Microscopic study of coupled heat and mass transport during unidirectional solidification of binary alloys—Parts I and II, Int. J. Heat Transfer 33 (1) (1990), 29–38 and 39–53.
[22] C. Koerber, M.W. Schiewe, K. Wollhover, Solute polarization during planar freezing of aqueous solutions, Int. J. Heat Mass Transfer 26 (8) (1983) 1241–1253.
[23] K. Wollhover, Ch. Koerber, M.W. Scheiwe, U. Hartmann, Unidirectional freezing of binary aqueous solutions: an analysis of transient diffusion of heat and mass, Int. J. Heat Mass Transfer 28 (1985) 761–769.
[24] R.L. Levin, E.G. Cravalho, C.G. Huggins, Water transport in a cluster of closely packed erythrocytes at subzero temperatures, Cryobiology 14 (1977) 549–558.
[25] R.L. Levin, The freezing of finite domain aqueous solutions: solute redistribution, Int. J. Heat Mass Transfer 24 (9) (1981) 1443–1455.
[26] R. Viskanta, M.V.A. Bianchi, J.K. Crister, D. Gao, Solidification processes of solutions, Cryobiology 34 (1997) 348–362.
[27] M.G. O'Callaghan, E.G. Cravalho, C.E. Huggins, An analysis of the heat and solute transport during solidification of an aqueous binary solution—I and II, Int. J. Heat Mass Transfer 25 (4) (1982), 553–561 and 563–573.
[28] C.V. Studholme, Modeling heat and mass transport in biological tissues during freezing, MS Thesis, Department of Mathematical Sciences, University of Alberta, Edmonton, Alberta, Canada, 1997.
[29] A. Karma, W.-J. Rappel, Phase-field simulation of three-dimensional dendrites: is microscopic solvability theory correct, J. Cryst. Growth 174 (1997) 54–64.
[30] Y.-T. Kim, N. Provatas, N. Goldenfeld, J. Dantzig, Universal dynamics of phase-field models for dendritic growth, Phys. Rev. E 59 (3) (1999) R2546–R2549.
[31] J.A. Warren, W.J. Boettinger, Prediction of dendritic growth and microsegregation patterns in a binary alloy using the phase-field method, Acta Metall. Mater. 43 (2) (1995) 689–703.
[32] X. Tong, C. Beckermann, A. Karma, Velocity and shape selection of dendritic crystals in a forced flow, Phys. Rev. E 61 (1) (2000) R49–R52.
[33] T.Y. Hou, J.S. Lowengrub, M.J. Shelley, Removing stiffness from interfacial flows with surface tension, J. Comput. Phys. 114 (1994) 312.
[34] Y.-T. Kim, N. Provatas, N. Goldenfeld, J. Dantzig, Computation of dendritic microstructure using a level-set method, Phys. Rev. E. 62 (2) (2000) 2471–2474.
[35] W.J. Boettinger, J.A. Warren, The phase-field method: simulation of alloy dendritic solidification during recalescence, Metall. Mater. Trans. A 27A (1996) 657–686.
[36] D.M. Anderson, G.B. McFadden, A.A. Wheeler, Diffuse interface methods in fluid mechanics, Ann. Rev. Fluid Mech. 30 (1998) 139–165.
[37] C.S. Peskin, Numerical analysis of blood flow in the heart, J. Comput. Phys. 25 (1977) 220–243.
[38] L.H. Ungar, M.J. Bennet, R.A. Brown, Cellular interface morphologies in directional solidification, Parts III and IV, Phys. Rev. B 31 (9) (1985), 5923–5930 and 5931–5940.
[39] W. Kurz, D.J. Fisher, Fundamentals of Solidification, third ed., Trans-Tech Publications, Switzerland, 1992.
[40] D.A. Kessler, J. Koplik, H. Levine, Pattern selection in fingered growth phenomena, Adv. Phys. 37 (1988) 255–339.
[41] C. Tu, C.S. Peskin, Stability and instability in the computation of flows with moving immersed boundaries: a comparison of three methods, SIAM J. Sci. Stat. Comput. 13 (1992) 1361.
[42] K.R. Diller, Intracellular freezing: effect of extracellular supercooling, Cryobiology 12 (1975) 480–485.
[43] H. Ishiguro, B. Rubinsky, Mechanical interactions between ice crystals and red blood cells during directional solidification, Cryobiology 31 (1994) 483–500.
[44] X. Tong, Effects of convection on dendritic growth, Ph.D. Thesis, University of Iowa, Department of Mechanical Engineering, Iowa City, IA, 1999.